International Journal of Multiphase Flow 34 (2008) 852–864

Contents lists available at ScienceDirect

International Journal of Multiphase Flow

journal homepage: www.elsevier.com/locate/ijmulflow

# Three-dimensional lattice Boltzmann simulations of droplet formation in a cross-junction microchannel

Long Wu [a,*], Michihisa Tsutahara [a], Lae Sung Kim [b], ManYeong Ha [b]

[a] Graduate School of Science and Technology, Kobe University, 1-1, Rokkodaicho Nada, Kobe 657-8501, Japan
[b] School of Mechanical Engineering, Pusan National University, San 30, Jangjeonn-Dong, Kumjung-Ku, Pusan 609-735, Republic of Korea

ARTICLE INFO

*Article history:*
Received 7 May 2007
Received in revised form 25 November 2007
Available online 17 March 2008

*Keywords:*
Immiscible fluids
Lattice Boltzmann method
Spurious velocity
Interfacial tension
Droplet formation
Cross-junction microchannel

ABSTRACT

An immiscible liquid–liquid multiphase flow in a cross-junction microchannel was numerically studied by the lattice Boltzmann method. An improved, immiscible lattice BGK model was proposed by introducing interfacial tension force based on the continuum surface force (CSF) method. The recoloring step was replaced by the anti-diffusion scheme in the mixed region to reduce the side-effect and control the thickness of the interface. The present method was tested by the simulations on a static bubble and the simulations of Taylor deformation. Laplace's law, spurious velocities, the thickness of interface, the pressure distribution and the small deformation theory were examined. It proves that our model is more advantageous for the simulation of immiscible fluids over the original immiscible lattice BGK model. The simulations of droplet formation in a cross-junction microchannel were performed and compared with the experiments. The numerical results show good agreements with the experimental ones for the evolution of droplet and the droplet size at various inlet velocities. Besides, a dimensionless analysis was carried out. The resulting droplet sizes depend on the Capillary number to a great extent under current conditions.



## 1. Introduction

Recently, droplet formation of two immiscible fluids in a microchannel has attracted extensive attentions due to its wide range of applications, such as food, cosmetic and pharmaceutical products (Anna et al., 2003; Doku et al., 2005). Microdroplets can be produced in such a multiphase system under certain conditions. The efficiency for generating microdroplets and properties of the liquid–liquid flow in microchannels are mainly influenced by the viscosity, the interfacial tension, the inlet velocities of two liquids and so on (Baroud and Willaime, 2004). The various parameters involved mean that optimizing the liquid–liquid multiphase flow in microreactors requires extensive experimental works. Therefore, numerical studies on such a system are indispensable to provide a reasonable and economically designed process.

It is well known that the variety and complexity of multiphase flows pose major challenges to a modeling approach. Accurate simulation of multiphase flow problems with a moving interface requires obtaining a sharp interface and recovering interfacial tension, which is often quite difficult for CFD researchers. Several techniques were developed in the last 25 years and can be classified into three main categories according to their physical and mathematical approaches: capturing (Lagrangian), tracking (Eulerian) and combined methods. Among the various approaches of multiphase flow simulation, the volume-of-fluid (VOF) (Hirt and Nichols, 1981), the level set method (Sussman et al., 1994) and the front-tracking method (Tryggvason et al., 2001) are known as useful and popular tools. Further new developments on capturing the interface include the particle-mesh method (Liu et al., 2005), the CIP method (Yabe et al., 2001) and so on. For the simulation of multiphase flow in microchannels, although the mentioned CFD packages can provide a general description of the flow patterns, simulations by traditional computation fluid dynamics are computationally expensive, partially due to the interface tracking costs.

In recent years, the lattice Boltzmann method (LBM) has developed into an alternative and powerful tool for complex fluids (McNamara and Zanetti, 1988; Higuera and Jiménez, 1989; Higuera and Succi, 1989; Chen and Doolen, 1998; Benzi et al., 1992). The fundamental idea of the LBM is to construct simplified kinetic models that incorporate the essential physics of microscopic processes. Macroscopic hydrodynamic behaviors, such as interface dynamics, naturally emerge as a result of this kinetics. The macroscopic dynamics of the fluid is the result of the collective behavior of microscopic physics. Several LB models for the simulation of multiphase flow have been developed. The first immiscible LBGK model (ILBGK) was proposed by Gunstensen et al. (1991) based on the R–K lattice gas model (Rothman and Keller, 1988) and modified by Grunau et al. (1993). Two kinds of colored particles (red and blue) are introduced for two-phases. The local flux

* Corresponding author.
*E-mail address:* long@exajapan.jp (L. Wu).

0301-9322/$ - see front matter © 2008 Elsevier Ltd. All rights reserved.
doi:10.1016/j.ijmultiphaseflow.2008.02.009

and color field (color gradient) are calculated and the maximum work of color flux against the color field is chosen to encourage the preferential grouping of same colors. Perturbation step is applied to realize the interfacial tension effect. An alternative multiphase LB model proposed by Shan and Chen (1993) which is based on the microscopic interactions between particles, and the latest version of this model can be found in the articles (Shan, 2006; Sbragaglia et al., 2007). The third LB model of multiphase flow was proposed by Swift et al. (1995) using a free-energy approach. The pressure tensor is consistent with the one derived from the free-energy function of nonuniform fluid. Although this model leaves the interface relatively wide, the spurious velocities decrease greatly.

All of the above LB models have their positive and negative properties. The use of one instead of the other is a question of the taste and of the application of interest. In the present study, the immiscible LBGK model (ILBGK) (Gunstensen et al., 1991) is used for two reasons. First, the sharp interface is maintained and the position of the interface can be known accurately. Second, this technique allows separating the treatment of interfacial tension effects from interface tracking, so that the value of the interfacial tension is easy to be calculated and adjusted. Although both properties above are advantageous when studying complex interface motion in confined and/or complex geometries, it should be noted that the original immiscible LBGK model still has some unphysical properties, such as spurious velocities and side-effect near the interface. To overcome these problems mentioned above, an improved immiscible LBGK model was proposed. With our model, the droplet formation in a cross-junction microchannel was numerically studied.

## 2. Numerical method

In this section, the original immiscible lattice BGK model (Gunstensen model (1991)) is reviewed briefly, and then two other variations are presented, including the Lishchuk model (2003) and the Latva-Kokko model (2005). Finally, our improved model is proposed.

### 2.1. Existing models

Gunstensen et al. (1991) reported the first immiscible lattice BGK model for multiphase flow. The two fluids denoted by different colors, red and blue, obey the lattice Boltzmann equation as

$$f_i^k(\mathbf{x}+\mathbf{e}_i, t+1) - f_i^k(\mathbf{x}, t) = \Omega_i^k(\mathbf{x}, t) \tag{1}$$

where, $f_i^k(\mathbf{x}, t)$ is the particle distribution function in the $i$th velocity direction for the $k$th fluid (red or blue) at position $\mathbf{x}$ and time $t$. $\mathbf{e}_i$ is the particle velocity of the $i$th direction. These particle distribution functions evolve according to Eq. (1). The collision operator, $\Omega_i^k(\mathbf{x}, t)$, is split into two parts. The first part denoted by $(\Omega_i^k)^1$ is the same as the BGK single-phase collision term and can be simplified as

$$(\Omega_i^k)^1 = -\frac{1}{\tau_k}[f_i^k(\mathbf{x}, t) - f_i^{k(\mathrm{eq})}(\mathbf{x}, t)] \tag{2}$$

where, $f_i^{k(\mathrm{eq})}(\mathbf{x}, t)$ is the equilibrium distribution function at position $\mathbf{x}$ and time $t$, and $\tau_k$ is the single-relaxation time for the $k$th fluid. The second part of the collision operator (perturbation step) is given as

$$(\Omega_i^k)^2 = A \mid \mathbf{G} \mid \cos 2(\theta_i - \theta_f) \tag{3}$$

where, $A$ is the adjustable interfacial tension parameter, $\theta_i$ is the angle of lattice direction $i$, and $\theta_f$ is the angle of the local gradient of the color field $\mathbf{G}$, which is defined as

$$\mathbf{G}(\mathbf{x}, t) = \sum_i \mathbf{e}_i[\rho_r(\mathbf{x}+\mathbf{e}_i, t) - \rho_b(\mathbf{x}+\mathbf{e}_i, t)] \tag{4}$$

where, $\rho_r$ and $\rho_b$ are densities of red and blue fluids, respectively. To prevent the two fluids from mixing with each other, the so-called recoloring step is applied. The basic idea of recoloring is to keep the interface sharp by reallocating $f_i^k(\mathbf{x}, t)$ in the mixed region at the collision step, so that colored particles cross the interface as few as possible. The colored particles are demixed according to the color field by maximizing the work of the color flux $\mathbf{q}(\mathbf{x},t)$ as follows

$$\mathbf{q}(\mathbf{x}, t) = \sum_i \mathbf{e}_i[f_i^r(\mathbf{x}, t) - f_i^b(\mathbf{x}, t)] \tag{5}$$

Through this "recolor" procedure, particles of each color tend to congregate together. Thus, the two fluids are forced to be immiscible.

Based on Gunstensen model, Lishchuk et al. (2003) modified the algorithm by replacing the perturbation step with a direct force term at the mixed region. This force term is used to recover the required pressure difference across the interface. Lishchuk's approach is a quite different process comparing with Gunstensen's method. It builds up the inner pressure of the droplet through a net body force acting on the interface. This step causes the interfacial length to decrease slightly and produces the desired interfacial tension as well. It has already been reported that Lishchuk's method provides much better drop isotropy and reduces spurious velocities significantly (Lishchuk et al., 2003). In addition (Halliday et al., 2007; Hollis et al., 2007), (i) Lishchuk's method has a controllable, directly input interfacial tension, (ii) it is much more stable than any of its competitors and able to reach much larger interfacial tensions (iii) in its latest form, with very-efficient, analytic component separation it is far simpler than either the Shan–Chen or free-energy methods, with much lower spurious velocities than the Shan–Chen method.

For Gunstensen's method, the recoloring step serves as an artificial anti-diffusion for separating two-phases by maximizing the work of the color flux. This kind of anti-diffusion has the adverse side-effect of disturbing the interface, which makes the interface profile to be zigzag. This may be caused by the lack of diffusion at the tangent of the interface. Thus, it is a natural idea to seek help in the replacement of the recoloring method with a moderate diffusion procedure. Recently, Latva-Kokko and Rothman (2005) reported a new scheme for the recoloring step by introducing an adjustable parameter $\beta$, which controls the strength of phase diffusion across the interface. Although Latva-Kokko's idea is used to fix the lattice pinning problem of the original immiscible lattice BGK model, its improvement can also be used for resolving the side-effect problem. Furthermore, this improved recoloring step is much easier to implement than the old one (Gunstensen model).

### 2.2. The present model

Based on above discussions, we modify the Gunstensen model by replacing the perturbation step with a direct forcing term at the mixed region with CSF model (Brackbill et al., 1992) and change the recoloring step by Latva-Kokko's anti-diffusion scheme (2005).

With the same notations, the lattice Boltzmann equation for the $k$th component can be written in the same form as Eq. (1), with the collision term being

$$\Omega_i^k(\mathbf{x}, t) = -\frac{1}{\tau_k}[f_i^k(\mathbf{x}, t) - f_i^{k(\mathrm{eq})}(\mathbf{x}, t)] \tag{6}$$

The 9-speed and 19-speed models are chosen in this study for two-dimensional and three-dimensional simulations, respectively. So that a suitable equilibrium distribution function takes the form

$$f_i^{k(\mathrm{eq})} = w_i \rho^k \left(1 + 3\mathbf{e}_{i\alpha}u_\alpha + \frac{9}{2}\mathbf{e}_{i\alpha}\mathbf{e}_{i\beta}u_\alpha u_\beta - \frac{3}{2}\mathbf{u}^2\right) \tag{7}$$

with $w_0 = 4/9$, $w_i = 1/9$for$i = 1, 2, 3, 4$, $w_i = 1/36$ for $i = 5, 6, 7, 8$ in two-dimensional simulations and $w_0 = 1/3$, $w_i = 1/18$, for$i = 1 \ldots 6$, $w_i = 1/36$,for$i = 7 \ldots 18$ in three dimensional simulations.

In Eq. (6), $\tau_k$ is the relaxation time for each kind of fluid. It is used to decide the value of the kinematic viscosity as

$$v = \frac{2\tau - 1}{6} \tag{8}$$

where $\tau$ is the relaxation time for the color blind fluid and is defined as $\tau = \sum \rho^k \tau_k / \rho$. These collision and relaxation rules lead to the following macroscopic mass and momentum equations (Rothman and Zaleski, 1977) as

$$\partial_t \rho + \nabla \cdot (\rho \mathbf{u}) = 0 \tag{9}$$

$$\partial_t \mathbf{u} + \mathbf{u} \cdot \nabla \mathbf{u} = -\frac{1}{\rho}\nabla p + v\nabla^2 \mathbf{u} \tag{10}$$

The densities $\rho^k$ for different phases, the total density $\rho$, momentum $\rho\mathbf{u}$ and pressure $p$ are obtained from the following equations:

$$\rho^k = \sum_{i=0}^{8} f_i^k = \sum_{i=0}^{8} f_i^{k(\mathrm{eq})} \tag{11}$$

$$\rho = \sum_k \rho^k \tag{12}$$

$$\rho\mathbf{u} = \sum_{i=0}^{8} \mathbf{e}_i f_i = \sum_{i=0}^{8} \mathbf{e}_i f_i^{\mathrm{eq}} \tag{13}$$

$$p = \frac{1}{3}\rho \tag{14}$$

In order to realize the interfacial tension effect, we force a local pressure gradient across the interface by an additional force term. A popular model for the interfacial tension force is the continuum surface force (CSF) model, which was developed by Brackbill et al. (1992). In the CSF model, the interfacial tension is interpreted as a continuous, three-dimensional effect across the interface, rather than as a pressure boundary condition on the interface. It is adopted in our model due to its easy implementation and high accuracy. After applying the interfacial tension force, the velocity $\mathbf{u}$ which is used for equilibrium distribution function is replaced by a new variable $\mathbf{u}^{\mathrm{eq}}$ defined as

$$\rho\mathbf{u}^{\mathrm{eq}} = \rho\mathbf{u} + \tau\mathbf{F} \tag{15}$$

where, $\tau$ is the relaxation time for the color blind fluid, the interfacial tension force $\mathbf{F}$ is added to the common velocity $\mathbf{u}$ and modeled as follows:

$$\mathbf{F} = \sigma\kappa\frac{\nabla C}{|\nabla C|} \tag{16}$$

where, $\sigma$ is the surface tension coefficient. The color field $C(\mathbf{x}, t)$ and interface curvature $\kappa$ are given as

$$C(\mathbf{x}, t) = \rho_{\mathrm{r}}(\mathbf{x}, t) - \rho_{\mathrm{b}}(\mathbf{x}, t) \tag{17}$$

$$\kappa = -(\nabla \cdot \hat{\mathbf{n}}) = \frac{1}{|\mathbf{n}|}\left[\left(\frac{\mathbf{n}}{|\mathbf{n}|}\cdot\nabla\right)|\mathbf{n}| - (\nabla\cdot\mathbf{n})\right] \tag{18}$$

where, $\hat{\mathbf{n}}(x)$ is the unit normal to the interface, and $\hat{\mathbf{n}}(\mathbf{x}) = \mathbf{n}(\mathbf{x})/|\mathbf{n}(\mathbf{x})|$. The normal vector $\mathbf{n}(\mathbf{x})$ is defined as

$$\mathbf{n}(\mathbf{x}) = \nabla C(\mathbf{x}) \tag{19}$$

The two parts inside the bracket of Eq. (18) can be calculated as follows:

$$(\nabla\cdot\mathbf{n})_{i,j} = \left(\frac{\partial n_x}{\partial x}\right)_{i,j} + \left(\frac{\partial n_y}{\partial y}\right)_{i,j} = \frac{1}{2\Delta x}[n_{x,i+1/2,j+1/2} + n_{x,i+1/2,j-1/2} - n_{x,i-1/2,j+1/2} - n_{x,i-1/2,j-1/2}] \tag{20}$$

$$+\frac{1}{2\Delta y}[n_{y,i+1/2,j+1/2} + n_{y,i-1/2,j+1/2} - n_{y,i+1/2,j-1/2} - n_{y,i-1/2,j-1/2}]$$

$$\left(\frac{\mathbf{n}_{i,j}}{|\mathbf{n}_{i,j}|}\cdot\nabla\right)|\mathbf{n}| = \left(\frac{n_x}{|\mathbf{n}|}\right)_{i,j}\left(\frac{\partial|\mathbf{n}|}{\partial x}\right)_{i,j} + \left(\frac{n_y}{|\mathbf{n}|}\right)_{i,j}\left(\frac{\partial|\mathbf{n}|}{\partial y}\right)_{i,j} \tag{21}$$

the normal vector $\mathbf{n}_{i,j}$ on the grid point and cell centered $\mathbf{n}_{i+1/2,j+1/2}$ are calculated by the following equations:

$$\mathbf{n}_{i,j} = \frac{1}{4}\left(\mathbf{n}_{i+1/2,j+1/2} + \mathbf{n}_{i+1/2,j-1/2} + \mathbf{n}_{i-1/2,j+1/2} + \mathbf{n}_{i-1/2,j-1/2}\right) \tag{22}$$

$$\mathbf{n}_{i+1/2,j+1/2} = \hat{\mathbf{x}}\left(\frac{C_{i+1,j}+C_{i+1,j+1}-C_{i,j}-C_{i,j+1}}{2\Delta x}\right) + \hat{\mathbf{y}}\left(\frac{C_{i,j+1}+C_{i+1,j+1}-C_{i,j}-C_{i+1,j}}{2\Delta y}\right) \tag{23}$$

After introducing the surface tension force, the recovered momentum equation becomes

$$\partial_t\mathbf{u} + \mathbf{u}\cdot\nabla\mathbf{u} = -\frac{1}{\rho}\nabla p + v\nabla^2\mathbf{u} + \mathbf{F} \tag{24}$$

The cumulative effect of the surface tension force is to produce an appropriate local step in pressure across the interface. Since this method does not conserve momentum locally, neither does the Shan–Chen method, we test the momentum conservation globally. For the direct force method, momentum non-conservation, creating a drift in the centre of mass of a high surface tension drop of radius 20 lattice units amounts to a drift of 1.0e−6 lattice units in 10,000 time steps. It is almost negligible.

The other improvement in our model is the modification of the recoloring step by implementing Latva-Kokko's anti-diffusion scheme. The crucial part of this solution is to allow the red and the blue fluids to moderately mix at the tangent of the interface and to keep the color distribution symmetric with respect to the color gradient. The following redistributions for the red and blue particles are used after the collision step.

$$f_i^{\mathrm{r}} = \frac{\rho_{\mathrm{r}}}{\rho_{\mathrm{r}}+\rho_{\mathrm{b}}}f_i + \beta\frac{\rho_{\mathrm{r}}\rho_{\mathrm{b}}}{(\rho_{\mathrm{r}}+\rho_{\mathrm{b}})^2}f_i^{\mathrm{eq}(0)}\cos\varphi \tag{25}$$

$$f_i^{\mathrm{b}} = \frac{\rho_{\mathrm{b}}}{\rho+\rho_{\mathrm{b}}}f_i - \beta\frac{\rho_{\mathrm{r}}\rho_{\mathrm{b}}}{(\rho_{\mathrm{r}}+\rho_{\mathrm{b}})^2}f_i^{\mathrm{eq}(0)}\cos\varphi \tag{26}$$

where, $f_i$ and $f_i^{\mathrm{eq}(0)}$ are the color blind distribution functions and zero-velocity equilibrium distribution functions going to $i$th direction, respectively. $\varphi$, defined in Eq. (27), is the angle between the color gradient and the particle velocities $\mathbf{e}_i$. $\beta$ is the parameter relating to the tendency of the two fluids to separate.

$$\cos\varphi|_i = \frac{\mathbf{G}\cdot\mathbf{e}_i}{|\mathbf{G}||\mathbf{e}_i|} \tag{27}$$

where $\mathbf{G}$ is the local gradient of the color field with the same definition as shown in Eq. (4). Without the last terms in Eqs. (25) and (26), red and blue particles would be distributed according to their numbers and there would be no tendency for the separation of the two fluids. Here, $\beta$ can take any value between 0 and 1 to control the diffusion and the width of the interface. When $\beta$ is larger than 1, there can be negative populations of particles. However, if the negative values are kept small, the stability is maintained (Latva-Kokko and Rothman, 2005). The relation between the thickness of interface and $\beta$ will be discussed in the next section.

## 3. Validation of the code

### 3.1. The simulations of a static bubble

The usefulness of our new model for easily and accurately simulating multiphase flow is demonstrated by the case of a static circular bubble with radius $R$. A 2D (in the $xy$-plane) simulations are performed in a $100 \times 100$ lattice cell system, and the periodic boundary conditions are employed.

First, we test Laplace's law, which is given as

$$\Delta P = P_{\text{in}} - P_{\text{out}} = \sigma / R \tag{28}$$

where $P_{\text{in}}$ and $P_{\text{out}}$ are the average pressures inside and outside the bubble, respectively. Simulations with different initial bubble radii were performed, and the final radius $R$ and the pressure differences were recorded. Fig. 1 is the plot of $\Delta P = P_{\text{in}} - P_{\text{out}}$ versus $1/R$. Here, the value of $\sigma$ is set to be 0.001. In Fig. 1, all points representing a radius from 8 to 20 almost fit a straight line. The pressure difference inside and outside the bubble is indeed proportional to the reciprocal of the radius in our simulations. This test shows that our method can correctly model the interfacial tension effect. In addition, it can be found that the slope ($\Delta P \cdot R = \sigma$) is quite close to the given interfacial tension $\sigma$. So, we can easily control the exact value of interfacial tension by present method.

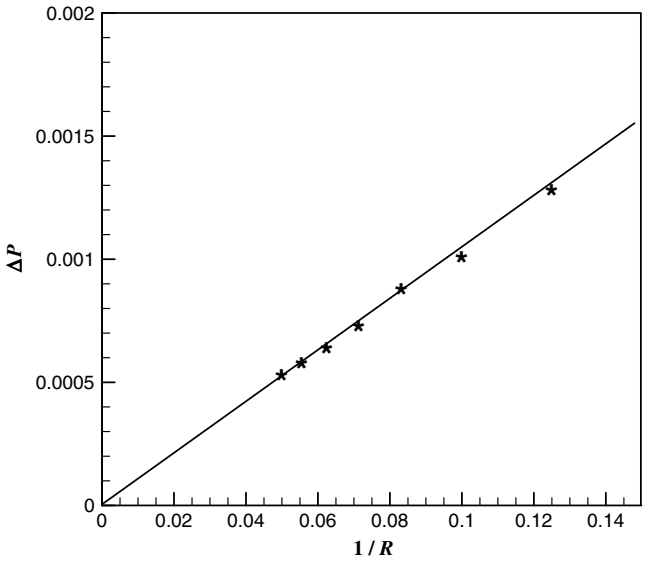


**Fig. 1.** Numerical confirmation of Laplace's law by the present method.

Second, the spurious velocities are examined for both the Gunstensen's model and the present model. Fig. 2 shows velocity vectors at the final stage of bubble evolution for (a) Gunstensen's model and (b) the present model. The interfacial tension coefficient $\sigma = 0.001$and the initial bubble radius $R = 15$ are used for both models. Although there may be some small relative fluctuations as time evolves, they present the typical velocity field. The magnitude of the velocities is represented by the length of the velocity vectors, for which the same scale is used in both models. The non-zero-velocity fields in pictures (a) and (b) represent the deviation of the results from the physical problem, especially the velocities near the interface region. These non-zero velocities are called spurious velocities. It can be found that the spurious velocities are much more serious in the Gunstensen model (Fig. 2a) than present model (Fig. 2b). The comparison is also given in Fig. 3 quantitatively. The variation of the velocity magnitude $|u|$with rotational angle is much smaller in our model.

Third, the pressure distributions are investigated. Fig. 4 shows the pressure distribution for (a) Gunstensen's model and (b) present model at $\sigma = 0.001$ and $R = 15$. The same scale is used for both models. The anisotropy in our method, characterized by the pressure distribution, appears to be much smaller than that in the Gunstensen's model, as shown in Fig. 4a and b. With the polar angle changing, the pressure distribution of our model almost keeps the same value as shown in Fig. 4b, but Gunstensen's model (Fig. 4a) shows larger variation. The variation in pressure distribution may cause the anisotropy of bubble behavior and induce large spurious velocities. The quantitative comparison of the pressure distributions is shown in Fig. 5. The anisotropy of the surface tension characterized by the variation of pressure with rotational angle appears to be much smaller than that in Gunstensen model. In addition, the present model obtains a continuous pressure distribution across the interface, while discontinuous distribution appears in Gunstensen's model.

Finally, the thickness of interface and its dependence on the parameter $\beta$ (see Eqs. (25) and (26)) are examined for the current

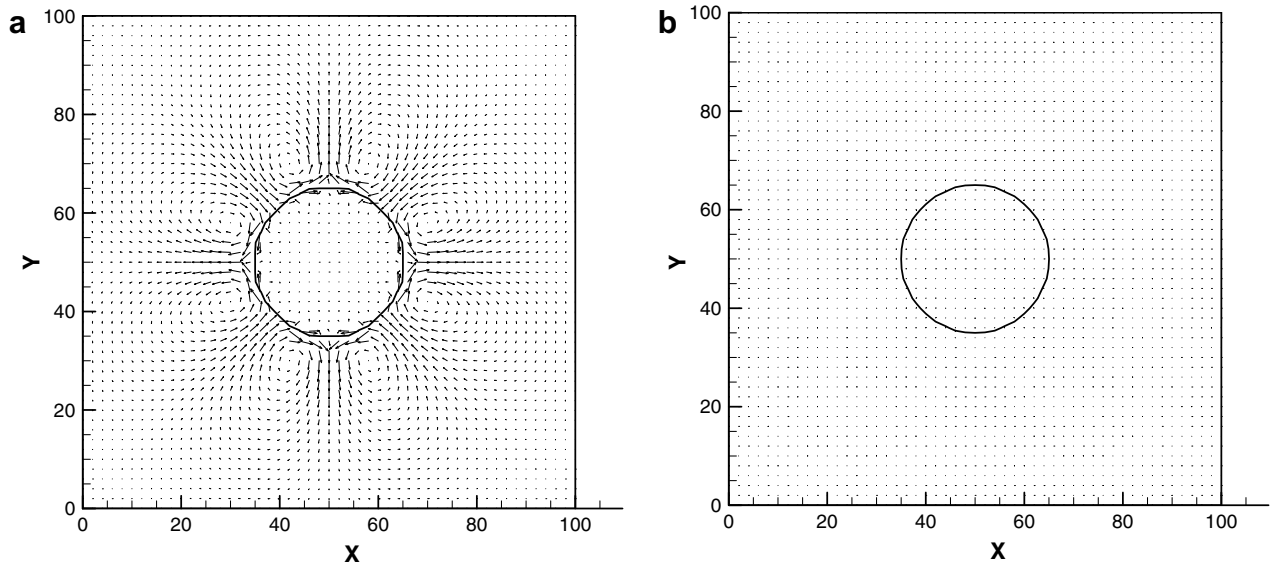


**Fig. 2.** The distribution of velocity vectors at $\sigma = 0.001$ and $R = 15$ for (a) Gunstensen's model and (b) present model.

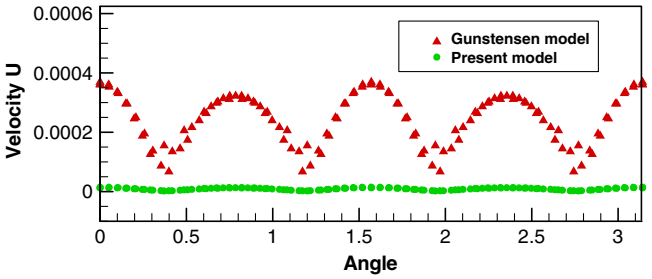


**Fig. 3.** Variation of the velocity magnitude with rotational angle around $R = 20.0$.

model. The surface tension coefficient $\sigma = 0.001$ and the initial bubble radius $R = 20$ are used here. Fig. 4 shows the thickness of interface against $\beta$ along the horizontal line at the middle of the computational domain ($y = 50$). From Fig. 6, we can find that the thickness of interface decreases significantly with the increase of $\beta$. A very sharp interface can be obtained at large $\beta$. Fig. 7 shows the interface profiles at various values of $\beta$. Four typical values of $\beta$ (0.5, 1.0, 1.5, 2.0) are used for discussion. When $\beta < 1$ (Fig. 7a), the interface profiles are very smooth but not so sharp. When $\beta \geqslant 1$ (Fig. 7b–d), the profiles become much sharper than that at small value of $\beta$. The thickness of interface can be decreased effectively by increasing the value of $\beta$. Generally, it is better to control the interface as sharp as possible, but when the interface becomes very sharp, minus density distribution (negative population of particles) will occur near the interface as shown in Fig. 7c and d ($\beta > 1$). Besides, when $\beta > 1$, the sharpness can not be improved efficiently by increasing $\beta$ as shown in Fig. 6. Also, the minus density distribution becomes significant at large $\beta$. This may lead to some very unreasonable results, since the density distributions are usually used for computing the average properties at the interface. Based on the above discussion, a moderate value $\beta = 1$ is used in the following study to get a sharp interface and prevent the minus density distribution.

### 3.2. Taylor deformation

As a dynamic problem, the simulations of Taylor deformation shown in Fig. 8 were performed to investigate the droplet deformation behavior of the two-phase code. A droplet is placed between two plates moving in opposite directions to obtain linear shear in the Stokes regime (small Reynolds number), and droplet deformation was studied as a function of the shear rate (expressed as the Capillary number). The definitions of the Reynolds number and the Capillary number are given as

$$Re = \frac{\dot{\gamma} R^2 \rho}{\eta} \tag{29}$$

$$Ca = \frac{\dot{\gamma} R \eta}{\sigma} \tag{30}$$

where $\dot{\gamma} = 2U/H$ is the shear rate (the velocity of the moving wall divided by the channel height), $R$ is the radius of the droplet, $\eta$ is viscosity, and $\sigma$ is the interfacial tension coefficient. The densities and viscosities are the same for both fluids in the present study (density ratio $\chi = \rho^r/\rho^b = 1.0$, and viscosity ratio $\lambda = \eta^r/\eta^b = 1.0$). Simulations were run in a system of $100 \times 50$ lattice cells, and for a droplet with

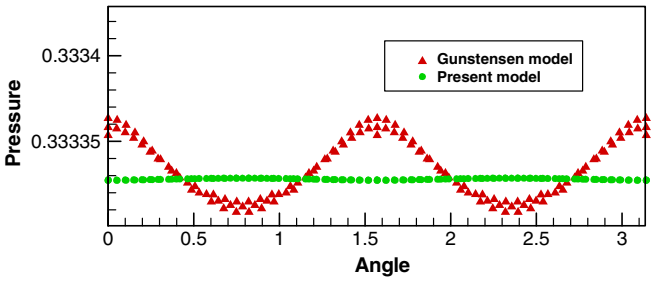


**Fig. 5.** Variation of the pressure with rotational angle around $R = 20.0$.

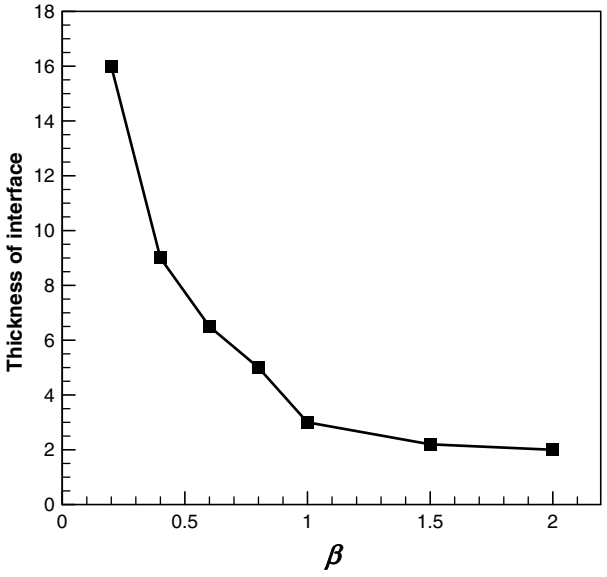


**Fig. 6.** The thickness of interface against various values of $\beta$.

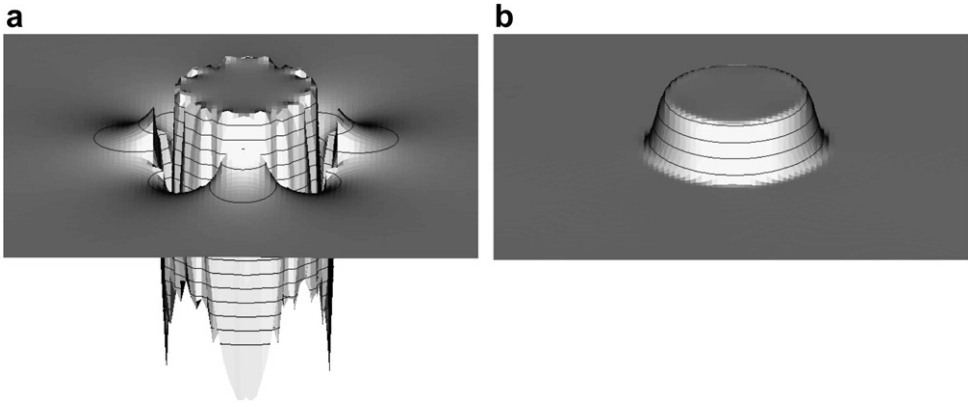


**Fig. 4.** The pressure distribution at $\sigma = 0.001$ and $R = 15$ for (a) Gunstensen's model and (b) present model.

a radius of 10 lattice cells. In the steady state, Taylor obtained a theoretical result for small deformation $D$ which is defined as

$$D = \frac{L-B}{L+B} = \frac{19\lambda+16}{16\lambda+16} = (35/32)Ca \tag{31}$$

Here $L$ and $B$ are the major and minor axis of the ellipse as shown in Fig. 8

Fig. 9 shows the comparison between our simulations and the theoretical prediction for $D$ versus $Ca$. From the figure one can see that the agreement between our numerical simulations and the theoretical result is excellent at small Capillary number. This agreement for small deformation is clear evidence that the numerical method performs well for dynamic problem. In Fig. 9, we also show the results for the cases with different Reynolds numbers, because the Reynolds number is also an important parameter to decide the flow pattern. In a small Reynolds number, the results of our simulations are more close to the theoretical line. In this case, the flow is almost decided by the Capillary number and agrees well with the small deformation theory in large extent. However, in higher Reynolds number, the deformation of the simulation is larger than the theoretical one for large Capillary number.

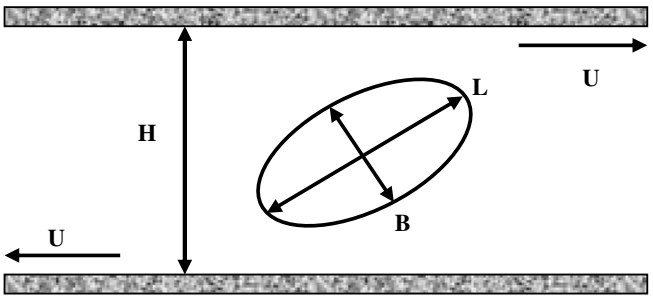


**Fig. 8.** Droplet deformation in a shear flow.

Parameter $\beta$ is checked in various values by this case. Here we show the examples for $\beta = 1.0$ and $\beta = 0.5$ in Fig. 9. It can be found that the results are not very sensitive to the thickness of the interface ($\beta = 1.0$ and $\beta = 0.5$). However, small $\beta$ (increase the thickness of the interface) will decrease the mobility of the interface and increase the resistance to deformation. The effect may become signif-

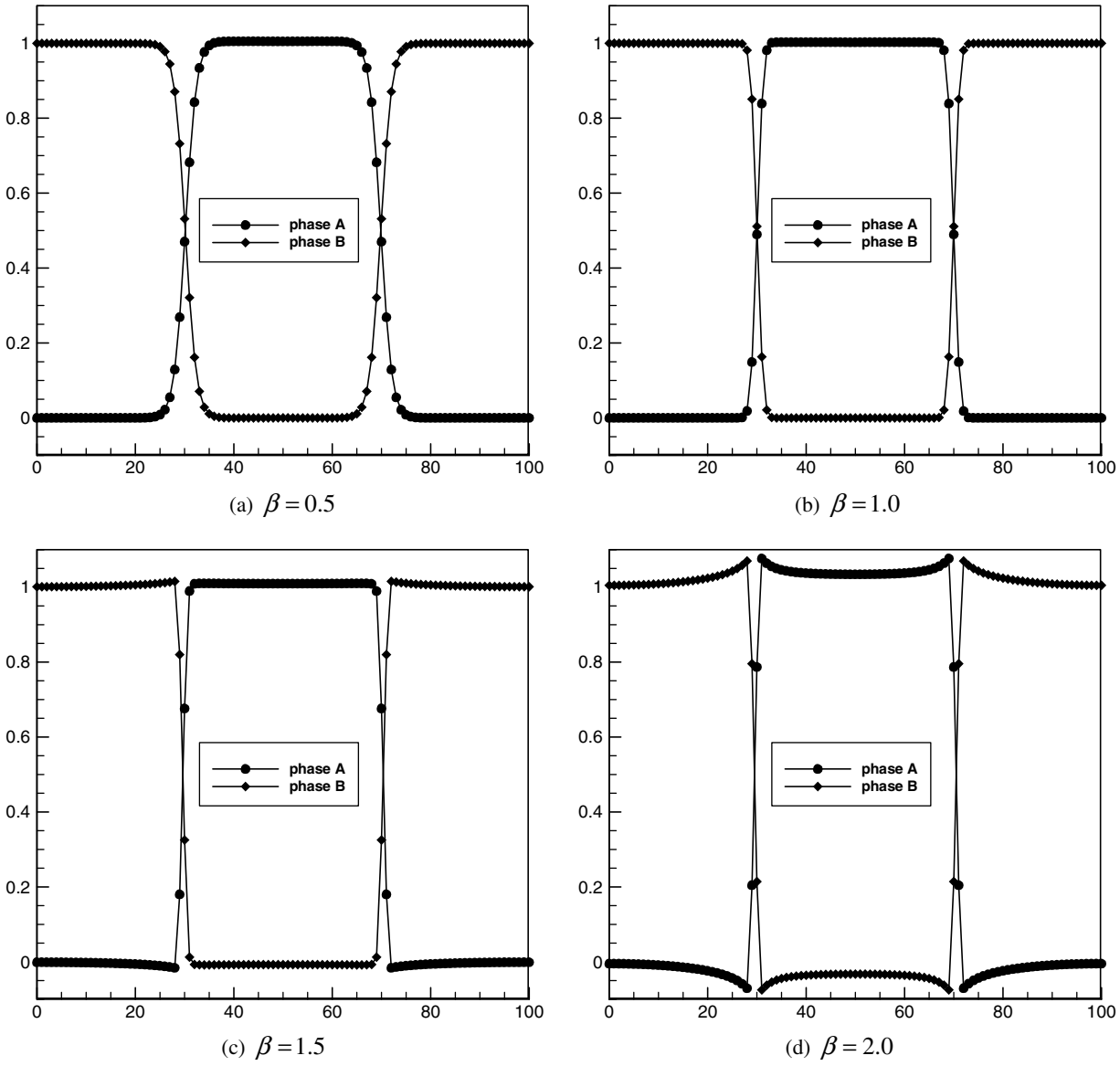


**Fig. 7.** The interface profiles at various values of $\beta$.

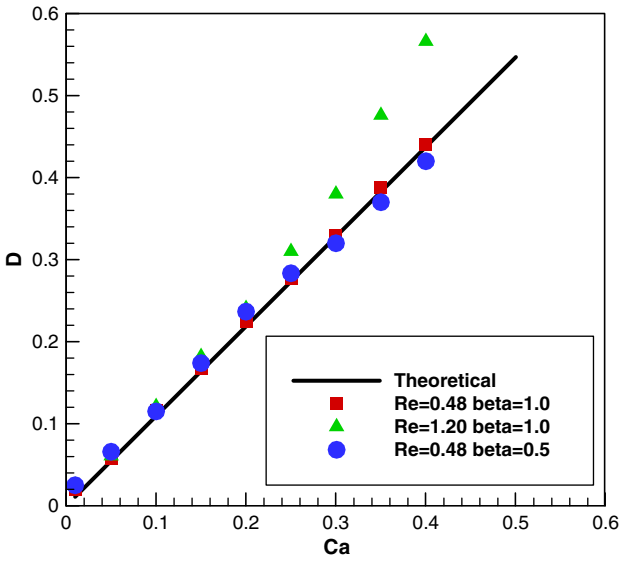


**Fig. 9.** Deformation parameter $D$ as a function of the Capillary number.

icant for small bubble case or very wide interface. In general, a sharp interface is desired in the multiphase flow simulations especially for many bubble system, in which the clear interface is necessary.

The comparison between the present model and Gunstensen model was also performed. Although the difference between two models in large Reynolds number and large Capillary number is not significant, the spurious velocities will become comparable with the main flow velocities for the cases of small Reynolds number and small Capillary number, and it may give a big error in the simulations. Fig. 10 shows the comparison of the flow field between two methods at $Re = 0.12$ and $Ca = 0.2$. It can be found that Gunstensen model give a large error, while our improved method can still predict the results very well.

Given the successful comparison with the Taylor result in the small deformation limit, we have performed the simulations at larger shear rates to investigate the ability of our model to adequately track the deforming interface to breakup. Fig. 11 shows snapshots of the evolution of the droplet under shear at $Re = 2.4$ and $Ca = 0.4$. The dimensionless time is defined as $t^* = 2Ut/H$. These pictures show that there is a considerable stretching and then a breakup occurs at the middle of the long and deformed droplet. From the simulations, we can find that the present model is expected to be suitable for describing droplet deformation and breakup.

## 4. Experiments and simulations of droplet formation

### 4.1. Model system and experimental setup

A cross-junction microchannel that had three inlet ports and single outlet was used in this study. This microchannel consisted of a main channel with a 200 μm width and two lateral channels

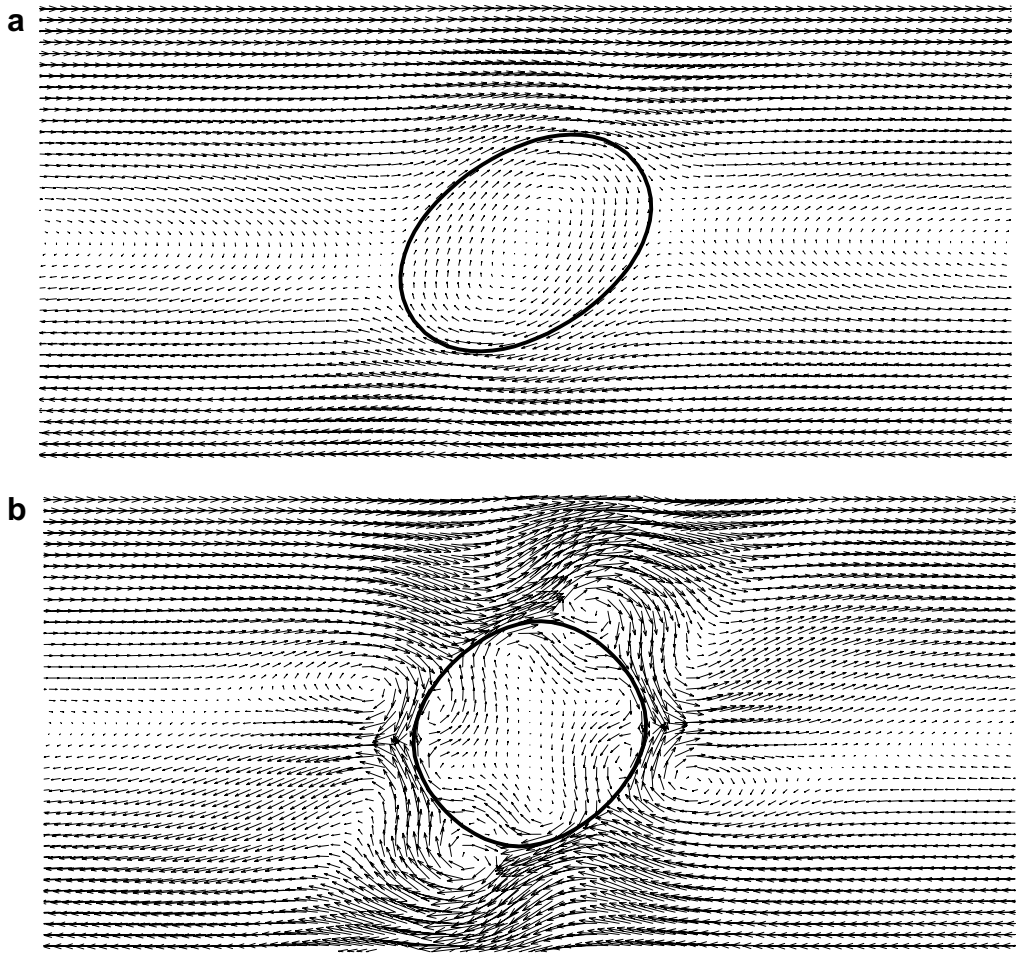


**Fig. 10.** Flow field of the droplet deformation at $Re = 0.12$ and $Ca = 0.2$ (a) the present model, (b) Gunstensen model.

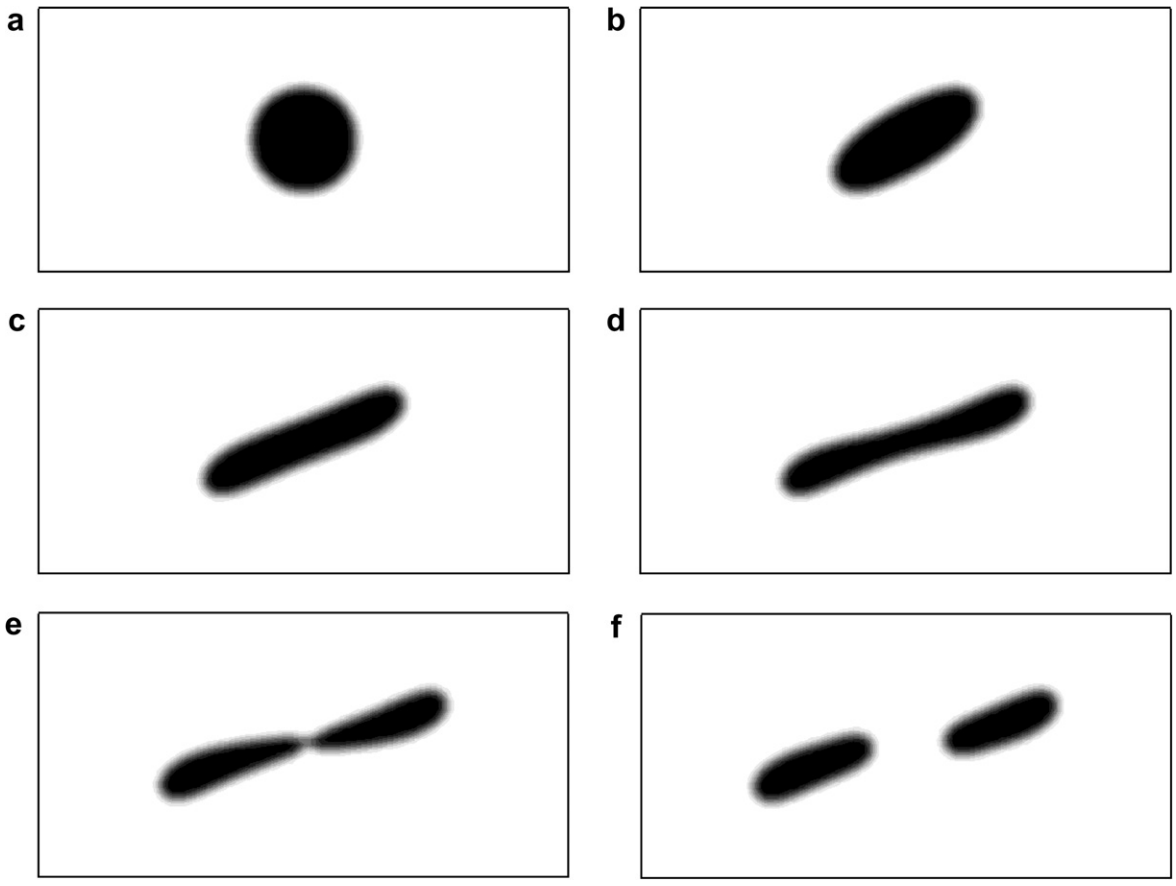


**Fig. 11.** Snapshots of the evolution of the droplet under shear at $Re = 2.4$ and $Ca = 0.4$ (a) $t^* = 0.2$, (b) $t^* = 2.0$, (c) $t^* = 4.0$, (d) $t^* = 6.0$, (e) $t^* = 7.5$, (f) $t^* = 8.0$.

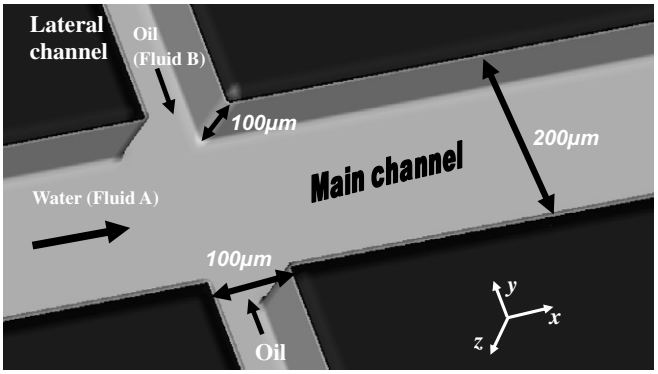


**Fig. 12.** Model system for droplet formation in a cross-junction microchannel.

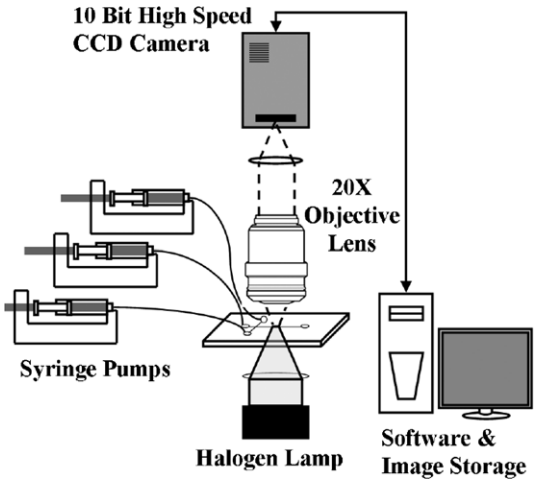


**Fig. 13.** Schematic of the system setup; the micro-PIV system consisted of a 10-bit highspeed CCD camera, a microscope, and syringe pumps.

with 100 μm widths as shown in Fig. 12. The depth was 100 μm through the whole channel. Fluid A (water-phase) was introduced into the main channel and fluid B (oil-phase) was injected into one of the lateral channels. The other lateral channel was used as the inlet channel for the water- or oil-phase fluid as the case may be (oil-phase was used in this study). As the water-phase, water with 3% PVA (viscosity, $\mu_A = 1.074 \times 10^{-2}$ Pa s; density, $\rho_A = 1.03 \times 10^3$ kg m$^{-3}$) was used. As the oil-phase, Freol ALPHA 10G (viscosity, $\mu_B = 2.441 \times 10^{-2}$ Pa s density, $\rho_B = 0.93 \times 10^3$ kg m$^{-3}$) was used. The interfacial tension is $\sigma = 0.03$ N m$^{-1}$. The magnitudes of the average inlet velocities are designated as $u_A$ for the water and $u_B$ for the oil. The velocity ratio is defined as $\alpha = u_A/u_B$. The channel was made of polydimethylsiloxane (PDMS) and was bonded to a glass plate by means of the plasma treatment using the $O_2$ plasma asher. However, the surface of PDMS structures can not only lose the hydrophobic characteristics but also can be extremely hydrophilic after the electrical discharges, e.g. the corona treatment in air or the plasma treatment. This loss of the hydrophobicity is a disadvantage or a problem to generate microdroplets. Hillborg (2001) reported about the loss and recovery of the hydrophobicity of the PDMS surface after exposure to electrical discharges. Hung and Lee (2004) suggested the heat treatment as a quick and efficient method for hydrophobicity recovery of PDMS, thus allowing

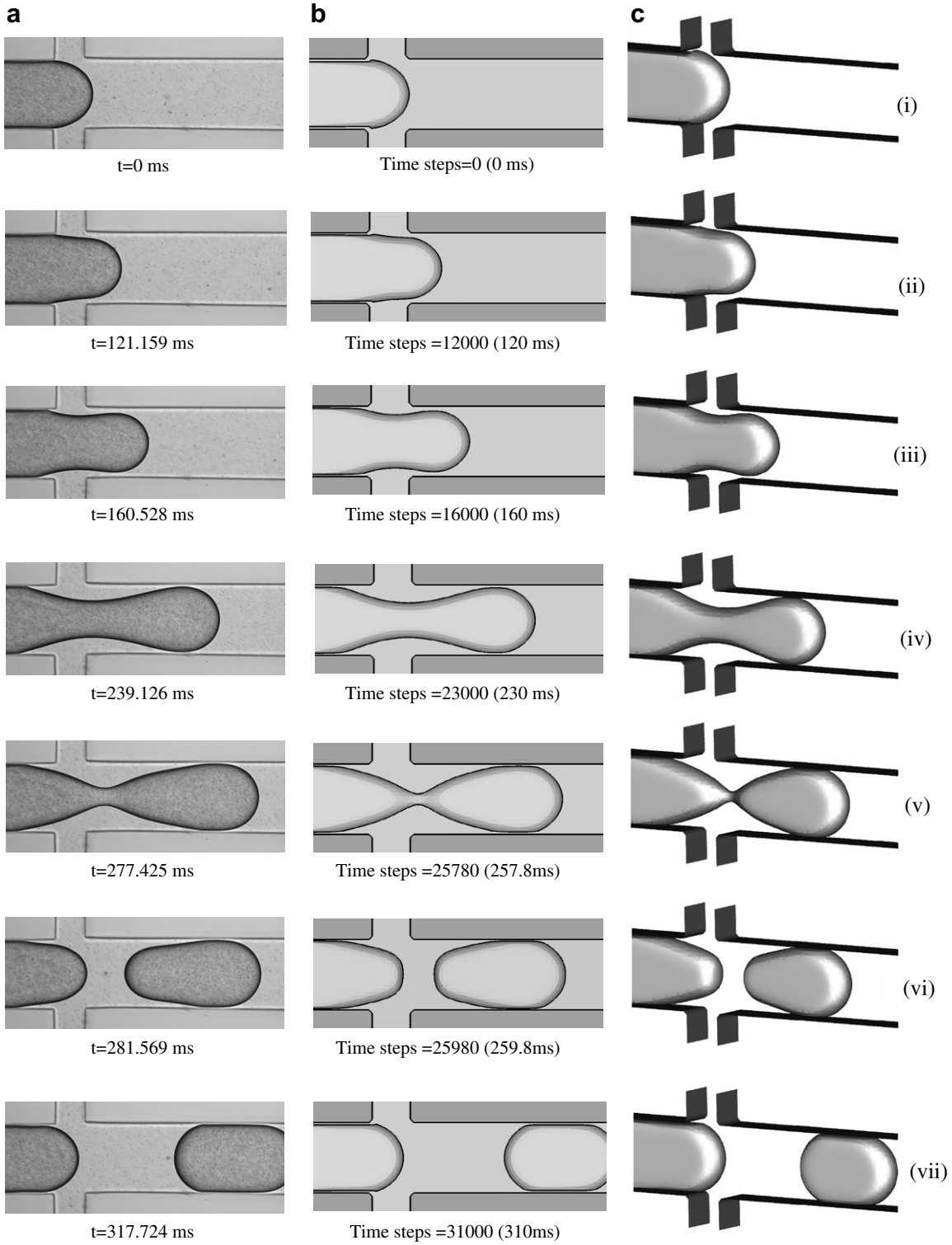


**Fig. 14.** A series of instantaneous states of droplet formation for (a) experimental results, (b) numerical results on $x$–$y$ plane and (c) numerical results of 3D profiles, at $u_A = 0.00084$ and $\alpha = 1/3$.

an alternative to toxic chemical assembling (e.g. silanization). The plasma-treated PDMS surface can recover the hydrophobicity through heat treatment. Hence, the PDMS channel was placed into a 120 °C oven for 72 h to recover the hydrophobicity after plasma bonding with a glass plate.

Fig. 13 shows the schematic illustration of the experimental set-up for the micro-PIV system for this study. The system consisted of a 10-bit highspeed CCD camera (1200hs, PCO), a microscope (BX51, Olympus), and syringe pumps. A 10-bit highspeed CCD camera with a 1280 × 1024 pixel resolution was used to get time-resolved velocity fields as a microdroplet was formed. A halogen lamp was focused and illuminated to a test section from the bottom of the microchannel. Then, shadows of particles were formed on the image plane, unlike using fluorescent lights emitted from particles.

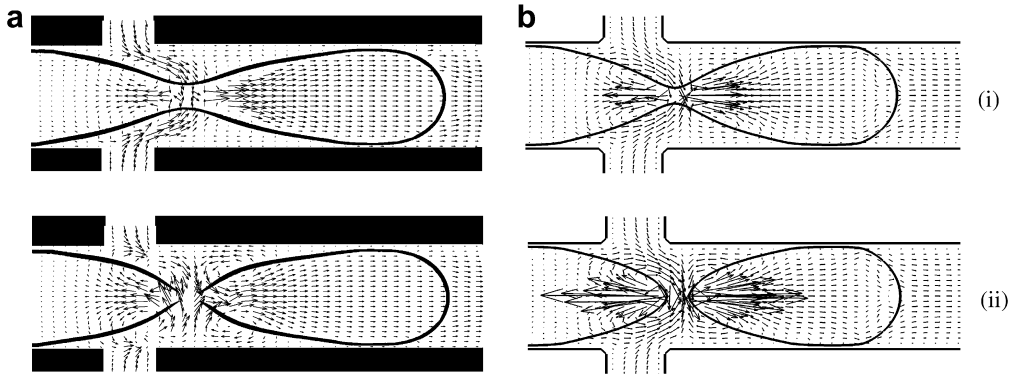


**Fig. 15.** The velocity fields obtained from (a) experiment and (b) simulation when droplet detaching, at $u_A = 0.00084$ and $\alpha = 1/3$.

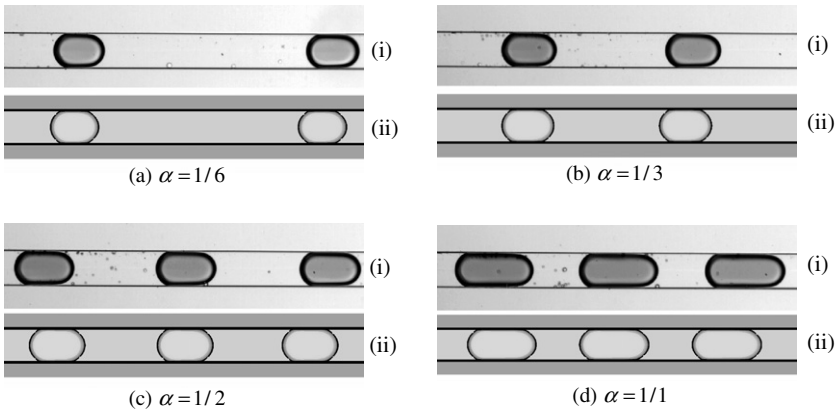


**Fig. 16.** Experimental (i) and simulated (ii) droplets at various velocity ratios for $u_B = 0.00252$.

Particles with 1 μm in diameter were seeded into the working fluids: water-phase and oil-phase fluids. The particles that were contained in an aqueous solution were dried and mixed with the oil-phase fluid to seed the particles into the oil-phase fluid. Ultrasonic treatment and filtering were performed to disperse particles and to eliminate lumps of several particles after mixing dried particles and the oil-phase fluid. To drive the flow, syringe pumps were used.

### 4.2. Numerical simulations

Such flows are described by a large number of parameters including the interfacial tension, the inlet velocity, the viscosity and variations in the density across the two fluids. Luckily, several parameters are naturally small. For instance, inertial effects are small comparing with viscous effects, yielding small Reynolds number which has a negligible effect on the formation of the droplet in microchannel (Tice et al., 2003). Gravitational effects will also generally be small comparing with interfacial tension, yielding a small Bond number. In contrast, the Capillary number ($Ca$) which describes the relative importance of viscosity and interfacial tension always dominates such flow system. The Capillary number is defined as $Ca = \mu U/\sigma$ where $\mu$ is the viscosity, $U$ is a typical velocity, and $\sigma$ is the interfacial tension. In the current study, the comparisons between experiment and simulation are performed based on Capillary number.

Furthermore, several authors have reported the importance of the interaction between the fluids with the walls. In order to generate structures of one fluid (fluid A) within another fluid (fluid B), fluid B (oil-phase) usually completely wets the walls of the microchannel while fluid A (water-phase) is non-wetting. In this study, we also concentrate on the cases where only one fluid (fluid B) wets the walls. The same idea in reference (Dupin et al., 2006) is employed to realize the wetness effect.

**Table 1**
Comparisons of droplet size obtained from experiment and simulation at various velocity ratios

| $\alpha$ | Length | | |
|---|---|---|---|
| | $L_{(i)}$ experiments (μm) | $L_{(ii)}$ simulations (μm) | Relative error $\lvert L_{(ii)} - L_{(i)} \rvert / L_{(i)}$ (%) |
| 1/6 | 275 | 270 | 1.82 |
| 1/3 | 300 | 295 | 1.67 |
| 1/2 | 310 | 300 | 3.33 |
| 1/1 | 410 | 390 | 5.00 |

($L_{(i)}$ is the length of the droplet for experiment and $L_{(ii)}$ is for simulation.)

#### 4.2.1. Comparisons with experiments

Detailed comparisons were made between experiments and simulations for the evolution of the droplet formation, the velocity vectors, and the droplets size. In the simulations, the same values of viscosities, interfacial tension and inlet velocities as those in experiments were used. Therefore, same Capillary numbers were obtained for simulations and experiments. The slight difference in mass densities between the experimental solutions is neglected in the simulations. Here $\rho_A = 1.0$, $\rho_B = 0.0$ in phase A and $\rho_A = 0.0$, $\rho_B = 1.0$ in phase B are used for the initial conditions. Both fluids are assumed to be incompressible, Newtonian and immiscible.

The simulations are performed in a $301 \times 61 \times 11$ cubic cell system and each cell size corresponds to 10 μm. This cell system was tested to be acceptable by comparing the results of a finer cell system of $601 \times 121 \times 21$(each cell size corresponds to 5 μm) in several different flow conditions. The relative error between the results of two cell systems is not more than 5%. No-slip boundary condition was applied for all the solid walls by the robust method of mid-link bounceback (Succi, 2001), which conveniently resolves the complex wall shapes and ensures the correct flux ratio by preventing the boundary "leakage error" in small velocity cases. Inlet and outlet fluxes and an outlet pressure (density) distribution were specified at every time step using an appropriate equilibrium $f_i^{(0)}(\rho, \mathbf{u})$ (Succi, 2001).

Fig. 14 shows a series of instantaneous states of droplet formation for (a) experimental results, (b) numerical results on $x$–$y$ plane and (c) numerical results of 3D profiles. The inlet velocity of water (fluid A) is $u_A = 0.00084$ and the velocity ratio is $\alpha = 1/3$. The time moment and corresponding time steps are given for each picture. It can be found that the droplet shape and size in the simulation agree well with the experimental results. Droplet formation proceeds in three stages, i.e. expansion (i)–(iv), necking (v) and figuration (vi)–(vii). The final droplet size is a result of these three stages. In the simulation, the droplet detaches a little earlier than that in experiment (v) and a smaller droplet is obtained (vii). For both experiment and simulation, the necking stage happened very fast within about 2–3 ms. In this stage, the radius of the throat becomes very small and a strong interfacial tension force "cuts" the fluid A suddenly.

Fig. 15 shows the velocity fields obtained from (a) experiment and (b) simulation when the droplet detaching. The inlet velocity of water (fluid A) is $u_A = 0.00084$ and the velocity ratio is $\alpha = 1/3$. Fluid A is split suddenly and a droplet is generated. Two symmetric vortices appear on the back of the generated droplet and on the front of to-be-dispersed phase. The simulated velocities agree with the experimental results in general. However, the simulation results show larger velocities than experiment around the break position. This may be because the computed curvature changes discontinuously in such a fast motion and leads to a strong variation of interfacial tension force.

Fig. 16 shows the snapshots of the droplet formation for experiments (i) and simulations (ii) at various velocity ratios (a) $\alpha = 1/6$, (b) $\alpha = 1/3$, (c) $\alpha = 1/2$, (d) $\alpha = 1/1$. Here, the inlet velocity $u_B = 0.00252$ is fixed. With the increase in the velocity ratio ($u_A$ increases), the droplet size becomes large. At small velocity ratio, fluid A breaks up easily and small droplets are obtained. It can be found that the velocity ratio is also one of the important factors to decide the size of generated droplets. The exact values of the droplet size (the length of the droplet) for experiments and simulations are listed in Table 1. For all the cases, the relative errors are below 5% and good agreements are obtained. With the increase in the velocity ratio, the relative error becomes large and the droplet size is underestimated by our simulations.

**Table 2**
Comparisons of droplet size obtained from experiment and simulation at various inlet velocities ($L_{(i)}$ is the length of the droplet for experiment and $L_{(ii)}$ is for simulations)

| $u_A$ (m/s) | Length | | |
|---|---|---|---|
| | $L_{(i)}$ experiments (μm) | $L_{(ii)}$ simulations (μm) | Relative error $\lvert L_{(ii)} - L_{(i)}\rvert / L_{(i)}$ (%) |
| 0.00042 | 275 | 270 | 1.82 |
| 0.000588 | 256 | 261 | 1.95 |
| 0.00084 | 225 | 235 | 4.44 |
| 0.00168 | 200 | 210 | 5.00 |

Fig. 17 shows the snapshots of the droplet formation for experiments (i) and simulations (ii) at various inlet velocities (a) $u_A = 0.00042$, (b) $u_A = 0.000588$, (c) $u_A = 0.00084$, (d) $u_A = 0.00168$, Here, the velocity ratio $\alpha = 1/6$ is fixed. With the increase in the inlet velocity, the obtained droplet size becomes small. The droplet shape and size are very similar for simulations and experiments. The exact values of the droplet size (the length of the droplet) for experiments and simulations are listed in Table 2. With the increase in the inlet velocity, the relative error becomes large and the droplet size is overestimated by our simulations. However, for all the cases, the relative errors are below 5%.

From the above comparisons between experiments and simulations (Figs. 14–17), a good ability of our model in simulating such a problem is proved.

*4.2.2. Influence of capillary number on droplet size*

Having validated the present model against experimental results, a series of simulations are performed at various interfacial tensions $\sigma(0.001 - 0.24)$ for three different inlet velocities $u_A$ (0.00084, 0.00168, 0.00336) at $\alpha = 1/3$. The viscosities used here for two fluids are $\mu_A = 0.01$ and $\mu_B = 0.024$, respectively. All above parameters appear in the Capillary number.

Fig. 18 shows the plot of simulation results of relative droplet size (the droplet length divided by the width of the main channel) against the Capillary numbers which is defined as $Ca = u_A \mu_A / \sigma$. The corresponding values of parameters for each curve lines are given in Table 3. It can be found that three curve lines almost overlap when $Ca < 0.005$, although the Reynolds number are different for various $u_A$. This proves that the flow mode is decided by the Capillary num-

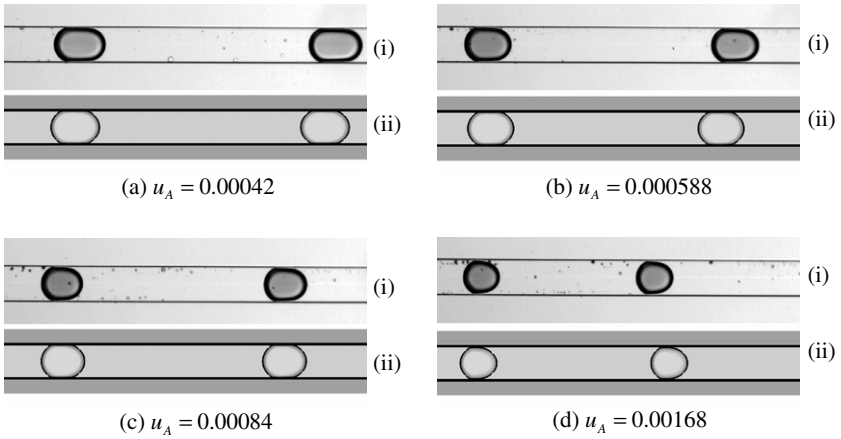


**Fig. 17.** Experimental (i) and simulated (ii) droplets for different inlet velocities $u_A$, at $\alpha = 1/6$.

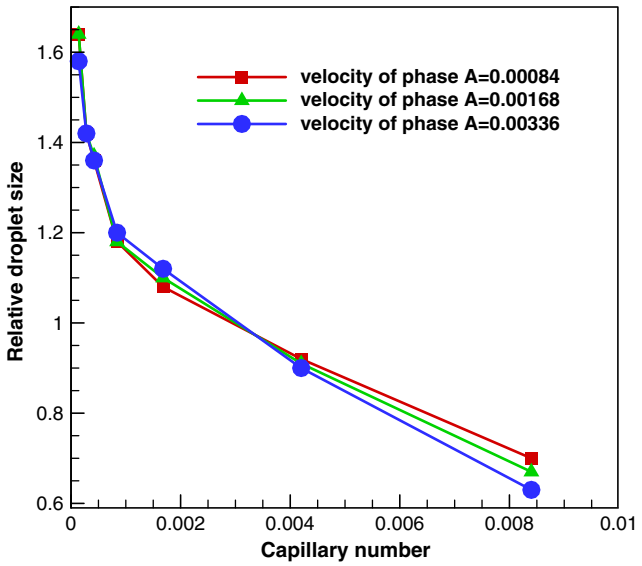


**Fig. 18.** Simulation results of relative droplet size against various Capillary numbers under three different inlet velocities at $\alpha = 1/3$.

**Table 3**
The corresponding values of various parameters for Fig. 12

| $Ca$ \ $u_A$ | 0.00084 | 0.00168 | 0.00336 |
|---|---|---|---|
| 0.00014 | 0.06 | 0.12 | 0.24 |
| 0.00028 | 0.03 | 0.06 | 0.12 |
| 0.00042 | 0.02 | 0.04 | 0.08 |
| 0.00084 | 0.01 | 0.02 | 0.04 |
| 0.00168 | 0.005 | 0.01 | 0.02 |
| 0.0042 | 0.002 | 0.004 | 0.008 |
| 0.0084 | 0.001 | 0.002 | 0.004 |

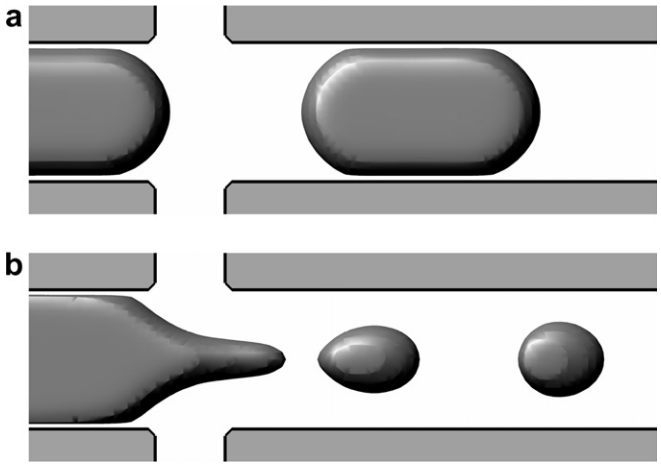


**Fig. 19.** The profiles of simulated droplets for (a) $Ca = 0.00014$ and (b) $Ca = 0.0084$ at $u_A = 0.00336$.

ber at $Ca < 0.005$. When the Capillary number reaches a large value ($Ca > 0.005$), three lines deviate from each other slightly and small droplets are generated under large inlet velocities. However, it seems that the flow is still decided by the Capillary number in general under the current conditions. Furthermore, the size of the generated droplet decreases when the Capillary number increases. Two samples of the profiles of simulated droplets are shown in Fig. 19.

Fig. 19 shows the profiles of simulated droplets for (a) $Ca = 0.00014$ and (b) $Ca = 0.0084$ at $u_A = 0.00336$. The phenomena are quite different for two different Capillary numbers. At $Ca = 0.00014$ (Fig. 19a), the droplet diameter is larger than the width of the channel and slugs are generated. In this case, the boundary conditions become important, especially the wetness properties. For $Ca = 0.0084$ (Fig. 19b), the generated droplets become small and are surrounded by the Fluid B. The influences of the channel geometry and boundary condition become less since the droplets do not touch the channel walls.

## 5. Conclusions

In the present work, an improved immiscible LBM model was proposed and validated by static bubble flow and Taylor deformation. Three-dimensional simulations were carried out on the immiscible two-phase flow in a cross-junction microchannel using this model. Comparisons with experimental data were made in detail. The influence of Capillary number on droplet formation was studied. The following conclusions were drawn:

(1) The recoloring step of original immiscible model was replaced by the anti-diffusion scheme. With the current method, the side-effect was suppressed, the continuous pressure distribution was obtained around the interface and the thickness of interface was easily controlled.
(2) By combining CFS model and immiscible LBGK model, the correct interfacial tension effect has been achieved. The exact value of interfacial tension can be controlled easily.
(3) The present method has the advantages for decreasing the spurious velocities and obtaining more reasonable pressure distribution across the interface over the original immiscible model.
(4) In the simulations of the droplet formation in the cross-junction microchannel, the flow pattern, droplet size and velocity vectors agree well with the experimental results.
(5) The flow patterns are mainly decided by the Capillary number in great extent under the current conditions.

## Acknowledgement

We would like to thank Dr. Ian Halliday from Sheffield Hallam University for the beneficial advice and valuable discussions.

## References

Anna, S.L., Bontoux, N., Stone, H.A., 2003. Formation of dispersions using "flow focusing" in microchannels. Appl. Phys. Lett. 82, 364–366.
Baroud, C.N., Willaime, H., 2004. Multiphase flows in microfluidics. C.R. Physique(Comptes Rendus) 5, 547–555.
Benzi, R., Succi, S., Vergassola, M., 1992. The lattice Boltzmann equation: theory and applications. Phys. Rep. 222, 145.
Brackbill, J.U., Kothe, D.B., Zemach, C., 1992. A continuum method for modeling surface tension. J. Comput. Phys. 100, 335–354.
Chen, S., Doolen, G.D., 1998. Lattice Boltzmann method for fluid flows. Ann. Rev. Fluid Mech. 30, 329–364.
Doku, G.N., Verboom, W., Reinhoudt, D.N., Berg, A.V.D., 2005. On-microchip multiphase chemistry – a review of microreactor design principles and reagent contacting modes. Tetrahedron 61, 2733–2742.
Dupin, M.M., Halliday, I., Care, C.M., 2006. Simulation of a microfluidic flow-focusing device. Phys. Rev. E 73, 0557011–0557014.
Grunau, D., Chen, S., Eggert, K., 1993. A lattice Boltzmann model for multiphase fluid flows. Phys. Fluids A 5, 2557–2562.
Gunstensen, A.K., Rothman, D.H., Zaleski, S., Zanetti, G., 1991. Lattice Boltzmann model of immiscible fluids. Phys. Rev. A 43, 4320–4327.
Halliday, I., Hollis, A.P., Care, C.M., 2007. Lattice Boltzmann algorithm for continuum multicomponent flow. Phys. Rev. E 76, 026708.
Hollis, A.P., Halliday, I., Law, R., 2007. Kinematic condition for multicomponent lattice Boltzmann simulation. Phys. Rev. E 76, 026709.
Higuera, F.J., Jiménez, J., 1989. Boltzmann approach to lattice gas simulations. Europhys. Lett. 9, 663.

Higuera, F.J., Succi, S., 1989. Simulating the flow around a circular cylinder with a lattice Boltzmann equation. Europhys. Lett. 8, 517.
Hillborg, H.C., 2001. Loss and recovery of hydrophobicity of polydimethylsiloxane after exposure to electrical discharges. Ph. D. Thesis. Department of Polymer Technology, Royal Institute of Technology, Stockholm, Sweden.
Hirt, C.W., Nichols, B.D., 1981. Volume of fluid (VOF) method for the dynamics of free boundary. J. Comput. Phys. 39, 201–225.
Hung, L.H., Lee, A.P., 2004. Optimization of droplet generation by controlling PDMS surface hydrophobicity. In: ASME International Mechanical Engineering Congress and RD&D Expo, Anaheim, California, IMECE 2004-61737.
Latva-Kokko, M., Rothman, D.H., 2005. Diffusion properties of gradient-based lattice Boltzmann models of immiscible fluids. Phys. Rev. E 71, 0567021–05670218.
Lishchuk, S.V., Care, C.M., Halliday, I., 2003. Lattice Boltzmann algorithm for surface tension with greatly reduced microcurrents. Phys. Rev. E 67, 0367011–03670115.
Liu, J., Koshizuka, S., Oka, Y., 2005. Ahybrid particle-mesh method for viscous, incompressible, multiphase flows. J. Comput. Phys. 202, 65–93.
McNamara, G.R., Zanetti, G., 1988. Use of the Boltzmann equation to simulate lattice-gas automata. Phys. Rev. Lett. 61, 2332–2335.
Rothman, D.H., Keller, J.M., 1988. Immiscible cellular-automaton fluids. J. Stat. Phys. 52, 1119–1127.
Rothman, D.H., Zaleski, S., 1977. Lattice Gas Cellular Automata. Cambridge University Press, Cambridge.
Sbragaglia, M., Benzi, R., Biferale, L., Succi, S., Sugiyama, K., Toschi, F., 2007. Generalized lattice Boltzmann method with multirange pseudopotential. Phys. Rev. E 75, 026702.
Shan, X., Chen, H., 1993. Lattice Boltzmann model for simulating flows with multiple phases and components. Phys. Rev. E 47, 1815–1819.
Shan, X., 2006. Analysis and reduction of the spurious current in a class of multiphase lattice Boltzmann models. Phys. Rev. E 73, 047701.
Succi, S., 2001. The Lattice Boltzamnn Equation for Fluid Mechanics and Beyond. Oxford–Clarendon, Oxford.
Sussman, M., Smereka, P., Osher, S., 1994. A level set approach for computing solutions to incompressible two-phase flow. J. Comput. Phys. 114, 146–159.
Swift, M.R., Osborn, W.R., Yeomans, J.M., 1995. Lattice Boltzmann simulations of nonideal fluids. Phys. Rev. Lett. 75, 830–833.
Tice, J.D., Song, H., Lyon, A.D., Ismagilov, R.F., 2003. Formation of droplets and mixing in multiphase microfluidics at low values of the Reynolds and the Capillary numbers. Langmuir 19, 9127–9133.
Tryggvason, G., Bunner, B., et al., 2001. A front-tracking method for the computations of multiphase flow. J. Comput. Phys. 169, 708–759.
Yabe, T., Xiao, F., Utsumi, T., 2001. The constrained interpolation profile method for multiphase analysis. J. Comput. Phys. 169, 556–593.